

1

Revision 1

2

The axial ratio of hcp Fe and Fe–Ni–Si alloys to the conditions of Earth’s inner core

3

4

Rebecca A. Fischer* and Andrew J. Campbell

5

Department of the Geophysical Sciences, University of Chicago, 5734 S Ellis Ave, Chicago, IL

6

60637, USA

7

*Corresponding author. Email: rfischer@uchicago.edu

8

9

Submitted to *American Mineralogist* (Building Planets), 9 September 2014

10

Revision 1, submitted 12 May 2015

11

12

Abstract

13

14

15

16

17

18

19

20

21

22

23

The Earth’s iron-rich inner core is seismically anisotropic, which may be due to the preferred orientation of Fe-rich hexagonal close packed (hcp) alloy crystals. Elastic anisotropy in a hexagonal crystal is related to its c/a axial ratio; therefore, it is important to know how this ratio depends on volume (or pressure), temperature, and composition. Experimental data on the axial ratio of iron and alloys in the Fe–Ni–Si system from 15 previous studies are combined here to parameterize the effects of these variables. The axial ratio increases with increasing volume, temperature, silicon content, and nickel content. When an hcp phase coexists with another structure, sample recovery and chemical analysis from each pressure-temperature point is one method for determining the phase’s composition and thus the position of the phase boundary. An alternate method is demonstrated here, using this parameterization to calculate the composition of an hcp phase whose volume, temperature, and axial ratio are measured. The hcp to hcp+B2

24 phase boundary in the Fe–FeSi system is parameterized as a function of pressure, temperature,
25 and composition, showing that a silicon-rich inner core may be an hcp+B2 mixture. These
26 findings could help explain observations of a layered seismic anisotropy structure in the Earth’s
27 inner core.

28

29

Introduction

30 In the upper part of the Earth’s iron-rich inner core, seismic waves traveling parallel to
31 the planet’s rotational axis propagate ~3% faster than waves traveling in the equatorial plane
32 (Morelli et al. 1986; Poupinet et al. 1983). Seismic data suggest the existence of layered
33 structures and hemispherical variations of this anisotropy (e.g., Irving and Deuss 2011a, 2011b;
34 Ishii and Dziewonski 2002, 2003; Lythgoe et al. 2014; Tanaka and Hamaguchi 1997). Numerous
35 mechanisms for explaining these properties have been considered (e.g., Alboussière et al. 2010;
36 Bergman 1997; Buffett and Wenk 2001; Jeanloz and Wenk 1988; Karato 1999; Reaman et al.
37 2011; Yoshida et al. 1996). This anisotropy is frequently attributed to preferred orientation of Fe-
38 rich alloy crystals in the inner core, due to iron’s strong single-crystal elastic anisotropy (Jeanloz
39 and Wenk 1988; Morelli et al. 1986; Stixrude and Cohen 1995). The *c/a* axial ratio of a
40 hexagonal crystal directly influences its elastic anisotropy (e.g., Steinle-Neumann et al. 2001;
41 Vočadlo et al. 2009; Wenk et al. 1988); therefore, the *c/a* ratio of preferentially aligned crystals
42 of a candidate core material can be related to the anisotropy of Earth’s inner core. For example,
43 *c/a* ratios of iron alloys can serve as input in calculations of elastic moduli or in models of core
44 anisotropy, as has previously been done in the case of pure hexagonal close packed (hcp) iron
45 (e.g., Steinle-Neumann et al. 2001; Vočadlo et al. 2009).

46 The subsolidus phase relations and equation of state of pure iron at high pressures have
47 been studied numerous times (e.g., Anzellini et al. 2013; Boehler et al. 2008; Dewaele et al.
48 2006; Jephcoat et al. 1986; Komabayashi et al. 2009; Ma et al. 2004; Mao et al. 1990; Ono et al.
49 2010; Sakai et al. 2011; Tateno et al. 2010; Uchida et al. 2001; Yamazaki et al. 2012) due to its
50 key geophysical applications. Some studies report a trend of the c/a ratio of hcp iron decreasing
51 with increasing pressure (Boehler et al. 2008; Dewaele et al. 2006; Jephcoat et al. 1986;
52 Yamazaki et al. 2012), while others report seemingly no trend, a very weak trend, or a trend that
53 changes with pressure (Jephcoat et al. 1986; Ma et al. 2004; Mao et al. 1990; Ono et al. 2010).
54 Similarly, some studies find that the c/a ratio of iron increases with increasing temperature
55 (Boehler et al. 2008; Sakai et al. 2011; Tateno et al. 2010; Yamazaki et al. 2012), in agreement
56 with most theoretical calculations (Belonoshko et al. 2003; Gannarelli et al. 2005; Modak et al.
57 2007; Sha and Cohen 2006; Steinle-Neumann et al. 2001; Wasserman et al. 1996), while others
58 do not (Ma et al. 2004). A few studies on iron (Boehler et al. 2008; Jephcoat et al. 1986) and Fe–
59 Ni–S alloy (Sakai et al. 2012) fit their room temperature data to a function describing how the
60 axial ratio changes with pressure, but it would be more useful to compile the extensive literature
61 on the c/a ratios of iron alloys into a single parameterization of their volume, temperature, and
62 compositional dependence; this is a goal of the present study.

63 Earth's inner core is known to contain several weight percent of nickel and of one or
64 more elements lighter than iron (Birch 1952; Jephcoat and Olson 1987). Silicon is one of the
65 leading candidates for comprising this light element component, based on its abundance,
66 presence in the metal of some chondritic meteorites, partitioning behavior, and non-chondritic
67 isotope ratio in the mantle (e.g., Allègre et al. 1995; McDonough 2003; Shahar et al. 2009).
68 Density functional calculations have indicated that Fe–Si hcp alloys can have significantly higher

69 elastic anisotropy than pure iron (Tsuchiya and Fujibuchi 2009), so it is important to consider the
70 composition of the alloy in addition to its structure when interpreting seismic anisotropy of the
71 inner core. Silicon-bearing alloys in the Earth's inner core may be an hcp+B2 mixture (Fischer et
72 al. 2013), depending on composition and temperature, which could offer an alternate explanation
73 for anisotropy. However, the exact phase stability of the hcp+B2 mixture of Fe–Si alloys remains
74 elusive, due to the difficulty of obtaining compositional measurements of coexisting phases in
75 experiments at the extreme pressures and temperatures of the Earth's core.

76 One of the goals of the present study is to combine some of the many available datasets
77 on the c/a ratio of pure iron and alloys in the Fe–Ni–Si system, to develop a single expression for
78 the variation in c/a ratio as a function of volume, temperature, and composition. This
79 parameterization can be used to calculate the compositions of the hcp component of hcp+B2
80 mixtures of Fe–9wt%Si (Fe–9Si) and Fe–16wt%Si (Fe–16Si) at high pressures using literature
81 data (Fischer et al. 2012, 2014). This will allow us to put better constraints on the Fe–Si phase
82 diagram at high pressures and temperatures, in particular the crystal structure of an Fe–Si alloy at
83 inner core conditions, and to enhance our understanding of anisotropy in Fe–Ni–Si alloys at core
84 conditions.

85

86

Methods

87 For our study of the c/a ratio of hcp iron, we selected numerous X-ray diffraction datasets
88 from among the studies on the equation of state and phase relations of iron. These datasets were
89 chosen based on their relatively smaller degree of scatter (see Discussion), the inclusion of
90 published c/a ratios, and general compatibility with other modern results on the trends of the c/a
91 ratio of iron with pressure and temperature. The studies used here consist of both diamond anvil

92 cell (Anzellini et al. 2013; Boehler et al. 2008; Dewaele et al. 2006; Fischer et al. 2011; Ono et
93 al. 2010; Sakai et al. 2011; Tateno et al. 2010) and multi-anvil press (Uchida et al. 2001;
94 Yamazaki et al. 2012) studies. We generally selected more recent datasets, which exhibit more
95 precise data due to improvements in experimental techniques.

96 These data were all collected using in situ synchrotron X-ray diffraction, using a variety
97 of different pressure standards and calibrations. Consideration of the pressure calibration is
98 critical when comparing results of different studies; here we largely circumvent this difficulty by
99 parameterizing c/a as a function of volume instead of pressure. In a few studies, only the
100 pressure, temperature, and c/a ratio was reported, and an equation of state was necessary to
101 determine the measured volume. Boehler et al. (2008) do not report unit cell volumes, and used
102 the ruby fluorescence pressure scale of Mao et al. (1986). We corrected their pressure
103 measurements to the ruby scale of Dorogokupets and Oganov (2007), which was calibrated
104 against the pressure scale of Dewaele et al. (2006). We then calculated the volume of iron in
105 their experiments from the corrected pressure and the reported temperature using the equation of
106 state of Dewaele et al. (2006). Likewise, Tateno et al. (2010) used the hcp iron equation of state
107 of Dubrovinsky et al. (2000) for their pressure calibration, so we used the Dubrovinsky et al.
108 (2000) equation of state to extract unit cell volumes from the pressures and temperatures reported
109 by Tateno et al. (2010).

110 To investigate the effects of nickel and silicon on the c/a ratio of hcp Fe alloys, we used
111 data from Fischer et al. (2014) on Fe–9Si, Lin et al. (2002a) on Fe–10Ni, Lin et al. (2002b) on
112 Fe–8Si, Sakai et al. (2011) on Fe–10Ni and Fe–5Ni–4Si, Komabayashi et al. (2012) on Fe–10Ni,
113 Tateno et al. (2012) on Fe–10Ni, and Tateno et al. (2015) on Fe–9Si and Fe–7Si. Lin et al.
114 (2002a, 2002b) do not report volumes, so the volumes were calculated using their reported

115 pressures and temperatures and the equations of state of pure iron (Dewaele et al. 2006) and Fe–
116 9Si (Fischer et al. 2014). The equation of state of Fischer et al. (2014) was calibrated against an
117 equation of state of B2 KBr (Fischer et al. 2012), which in turn was calibrated against the
118 equation of state of Dewaele et al. (2006), so these scales should be consistent.

119

120

Results

121 The data we have compiled on the c/a ratio in hcp Fe–Ni–Si alloys are listed in
122 Supplemental Table S1. It includes 928 measurements taken from 15 different studies, listing the
123 c/a ratio, its uncertainty where available, volume, temperature, lattice parameter a , and mole
124 fraction of silicon and nickel for each measurement. There are 632 measurements of pure Fe, 100
125 of approximately $\text{Fe}_{0.9}\text{Ni}_{0.1}$ (Fe–10Ni), 6 of $\text{Fe}_{0.88}\text{Ni}_{0.04}\text{Si}_{0.08}$ (Fe–5Ni–4Si), 10 of $\text{Fe}_{0.88}\text{Si}_{0.12}$ (Fe–
126 6.5Si) and 180 of approximately $\text{Fe}_{0.84}\text{Si}_{0.16}$ (Fe–9Si). Data on pure Fe span ~6–340 GPa
127 (Dewaele et al. 2006) and 300–4890 K, data on Fe–Ni alloys span ~25–340 GPa and 300–4700
128 K, and data on Fe–Si alloys span ~13–407 GPa and 300–5910 K.

129 Figure 1a shows the c/a ratio of pure iron from numerous studies as a function of volume
130 and temperature (Anzellini et al. 2013; Boehler et al. 2008; Dewaele et al. 2006; Fischer et al.
131 2011; Ono et al. 2010; Sakai et al. 2011; Tateno et al. 2010; Uchida et al. 2001; Yamazaki et al.
132 2012). This figure illustrates that there is still considerable scatter within and between the
133 datasets shown here; however, there is even greater scatter in the older datasets not chosen for
134 inclusion in this study (e.g., Jephcoat et al. 1986; Ma et al. 2004; Mao et al. 1990). Regardless,
135 Figure 1a demonstrates a trend of increasing c/a ratio with increasing volume and with
136 increasing temperature. Similarly, the c/a ratios of hcp Fe–Ni alloys containing ~10 wt% Ni are
137 shown in Figure 1b (Komabayashi et al. 2012; Lin et al. 2002a; Sakai et al. 2011; Tateno et al.

138 2012). Figure 1c shows the c/a ratio of hcp Fe–9Si where it does not coexist with any other
139 phases (Fischer et al. 2014; Lin et al. 2002b; Tateno et al. 2015). The c/a ratio in these alloys
140 increases with both volume and temperature, similar to that of pure iron (Figure 1a).

141 If the axial ratio of hcp iron approaches its ideal value of 1.633 at core conditions, this
142 could prevent anisotropy in the inner core by preferential alignment of hcp crystals (e.g., Steinle-
143 Neumann et al. 2001). However, the data in Figure 1 indicate that the temperature dependence at
144 inner core conditions is not strong enough for the c/a ratio to approach this value for pure Fe or
145 Fe–Ni–Si alloys.

146 Figure 2 illustrates the c/a ratio of Fe–9Si changing as a function of temperature during a
147 single heating cycle at ~145 GPa (Fischer et al. 2014). For reference, data on the c/a ratio of pure
148 iron from several studies at ~130–155 GPa are also shown (Anzellini et al. 2013; Boehler et al.
149 2008; Fischer et al. 2011; Tateno et al. 2010). Within experimental precision, the temperature
150 dependence of the measured axial ratio at this pressure appears to be the same for Fe–9Si and for
151 pure Fe, since the trends in Figure 2 are parallel. The c/a ratio of the alloy is higher than that of
152 iron by ~0.009 at these conditions.

153

154

Discussion

Axial ratios as a function of volume, temperature, and composition

155 The c/a ratio of an Fe–rich hcp alloy is a function of volume (V), temperature (T), and
156 composition (X_{Si} , X_{Ni}). Using the data shown in Figure 1 and listed in Table S1, we have
157 parameterized its dependence on these variables in the Fe–Ni–Si system as an unweighted linear
158 fit to the data. We found the best fit to the compiled data with the following relationship:

159
160
$$c/a = 1.551 + (-2.6 \times 10^{-6}) * T + 0.0094 * V + (1.5 \times 10^{-6}) * T * V +$$

161
$$(4.4 \times 10^{-4}) * X_{Si} + (2.8 \times 10^{-4}) * X_{Ni} \quad (1)$$

162 with T in Kelvin, V in cm^3/mol , and X_{Si} and X_{Ni} in mole fraction (e.g., $X_{Si} = X_{Ni} = 0$ for pure iron
163 and $X_{Si} = 16$ for Fe–9Si). The variance-covariance matrix describing this fit is shown in
164 Supplemental Table S2. Based on the amount of scatter in the data, it was not justifiable to fit
165 any additional terms to Equation 1; for example, allowing the temperature dependence of the c/a
166 ratio to vary with composition did not significantly improve the quality of the fit.

167 Figures 1 and 2 contain curves calculated from this parameterization compared to the
168 data. As volume increases, the c/a ratio increases. The c/a ratio always increases with increasing
169 temperature, but this effect is strongest at higher volumes, and becomes weaker with decreasing
170 volume. Based on the available data, we could not justify fitting any more than linear
171 compositional terms. This implies that the axial ratios of alloys in the Fe–Ni–Si system have
172 similar volume and temperature dependences, regardless of composition, and are simply shifted
173 from each other based on their silicon and nickel contents.

174 Residuals to this fit from various studies are illustrated as a function of temperature and
175 volume in Figure 3, which demonstrates the adequacy of Equation 1 to describe the data. The
176 root mean squared (rms) average misfit between measured c/a ratios and those calculated from
177 Equation 1 is 0.004 for the studies included in the fit, with the rms misfits for individual datasets
178 ranging from 0.002 to 0.007. While these misfits are small in absolute value, they equate to
179 ~10% of the range seen in the data. In comparison, previous studies not included in the fit due to
180 a higher degree of scatter exhibit an estimated 2σ variation of > 0.01 . The c/a ratio is likely
181 affected by deviatoric stresses as well, which may explain the greater misfit in the 300 K data,
182 but in this analysis we estimate that high experimental temperatures are sufficient to relax the
183 hcp alloy and minimize deviatoric stress effects on the axial ratio.

184 Sakai et al. (2012) studied the effects of sulfur on the c/a ratio of hcp iron–nickel alloys at
185 300 K and high pressures. They found an approximately linear relationship between c/a and
186 pressure, which is different from the trend we observe in this more extensive cross-study
187 analysis. Their data indicate that adding 2.8 mol% S to Fe–9Ni alloy lowers the c/a ratio by
188 ~ 0.005 , though this varies with pressure due to the different pressure trend reported in their
189 study.

190

191 **Using the axial ratio of an Fe–Si alloy to determine its composition**

192 Our fit to the available literature data relates the c/a ratio, temperature, volume, and
193 composition of an alloy in the Fe–Ni–Si system. Therefore, in circumstances where independent
194 measurements of the c/a ratio, temperature, and volume of an Fe–Si alloy are available from X-
195 ray diffraction and spectroradiometry (or thermocouple sensor), this parameterization may be
196 used to calculate the alloy’s silicon content. In Fe–9Si and Fe–16Si, coexisting hcp+B2
197 structures are observed in some regions of phase space (Fischer et al. 2012, 2013). When two
198 Fe–Si phases are present, silicon partitions between them as a function of pressure and
199 temperature such that the compositions of the phases are unknown without sample recovery and
200 analysis from each P - T point of interest. The method presented here provides an alternative to
201 this restrictive process.

202 Figure 4 illustrates the results of this method, applied to synchrotron X-ray diffraction
203 measurements of Fe–Si alloys at 125 and 145 GPa. At each P - T point, we have used the
204 measured c/a ratio and Equation 1 to calculate the composition of the hcp phase that coexists
205 with the B2 structure, thus providing the composition along the hcp to hcp+B2 phase boundary.
206 We used data on Fe–9Si (Fischer et al. 2014) and Fe–16Si (Fischer et al. 2012), which are shown

207 in Figure 4 to be mutually consistent in their definitions of the phase boundary. The in situ
208 crossing of this phase boundary determined in Fe–9Si (Fischer et al. 2013) agrees with the
209 calculated compositions along the phase boundary within uncertainty at both pressures, verifying
210 our results. As is evident in Figure 4, this method is most useful when applied to data at
211 temperatures far from any observed phase boundary crossings, to best constrain the slope of the
212 boundary in T - X space.

213 Under experimental P - T conditions where an hcp Fe–9Si alloy does not coexist with any
214 other phase, its composition is the same as the bulk starting composition. We have compared its
215 known composition under these conditions to its composition calculated from its c/a ratio to
216 determine the precision of our method, finding a root mean square (rms) misfit of 3.9 wt%
217 silicon, based on all 147 high temperature measurements spanning 45–407 GPa (Fischer et al.
218 2014; Lin et al. 2002b; Tateno et al. 2015). We take this as an estimate of the uncertainty in the
219 calculations shown in Figure 4. The misfit might be greater at different compositions; since the
220 fit is based only on alloys with up to 9 wt% Si, we caution against its extrapolation to alloys with
221 considerably higher silicon contents.

222 Figure 4 illustrates that at temperatures approaching the eutectic temperature in the Fe–
223 FeSi system (3700(300) K at 125 GPa, 3900(300) K at 145 GPa) (Fischer et al. 2012, 2013), the
224 composition of hcp alloy that coexists with B2 alloy nearly approaches pure iron. This result is
225 consistent with ab initio studies, which find that hcp is the stable phase of iron at inner core
226 conditions but that there is a small energy difference between hcp and bcc structures, with bcc
227 stabilized by the addition of silicon (Vočadlo et al. 2003). At these pressures, eutectic melting
228 from an hcp+B2 mixture is likely over a wide range of silicon contents in Fe–Si alloys,
229 extending down to low silicon contents. The slopes we find for this phase boundary (Figure 4)

230 are slightly shallower than the boundaries reported in Fischer et al. (2013), whose slopes were
231 less well constrained. This result extends the stability of the B2 structure to lower silicon
232 contents at high temperatures, which implies that partial melting of Fe–Si alloys can produce a
233 substantial density contrast between the melt and coexisting Si-poor metal. This concept is
234 illustrated schematically in Figure S1. A 4.5–7% density contrast is observed at Earth’s inner
235 core boundary (Dziewonski and Anderson 1981; Kennett et al. 1995; Masters and Gubbins
236 2003), which represents the point at which solid Fe-rich alloy crystallizes from a metallic melt.
237 At one bar the melting loop in the Fe–Si system is too narrow to explain such a large density
238 contrast, but the much larger compositional loop at high pressures, shown in this study and in
239 Fischer et al. (2013), supports the possibility that silicon could be the major light element in the
240 core, consistent with the seismological constraints.

241

242 **Calculation of the Fe–Si phase diagram in the inner core**

243 Since our parameterization of the relationship between volume, temperature, c/a ratio,
244 and silicon content spans a large P - T range up to >400 GPa and >5900 K, it can be used to
245 calculate phase boundaries at inner core conditions. The inner core is at pressures of 329–364
246 GPa (Dziewonski and Anderson 1981) and is thought to be nearly isothermal (e.g., Pozzo et al.
247 2014). The temperature of the inner core is anchored at the inner core–outer core boundary
248 (ICB), which is at the liquidus of the core’s Fe-rich alloy. An extrapolation of recent results on
249 the melting of pure Fe suggest that it melts at ~6200 K at 329 GPa (Anzellini et al. 2013). At
250 pressures of 50–140 GPa, we observe a ~200 K melting point depression in Fe–Si alloys relative
251 to pure Fe (Fischer et al. 2012, 2013). Consequently, we use here an estimated ICB temperature
252 of ~6000 K for an Fe–Si core. This is an approximate lower bound on the ICB temperature of a

253 postulated Fe–Si core, because the melting data in the Fe–Si system are for the solidus and the
254 inner core is crystallizing along the liquidus.

255 To determine the phase diagram of an Fe–Si core, we first calculated the hcp to hcp+B2
256 phase boundary based on experimental data from thirteen heating cycles ranging from 45 to 200
257 GPa. We used *c/a* ratios from Fischer et al. (2012, 2014), following the method described above
258 and illustrated in Figure 4 at two different pressures. We then performed a weighted linear fit to
259 these results, describing the relationship between pressure, temperature, and silicon content along
260 the phase boundary. The resultant hcp to hcp+B2 boundary in the Fe–Si system is described by
261 the equation:

$$262 \quad \text{wt\% Si} = 16.15 - 0.00555 * T + 0.0520 * P \quad (2)$$

263 where temperature *T* is in Kelvin, pressure *P* is in GPa, and silicon content is in weight percent.

264 A term describing the pressure dependence of the slope (constant**P***T*) was not used, as it was
265 found to be statistically insignificant at the 90% confidence level. The variance-covariance
266 matrix describing this fit is shown in Supplemental Table S3. The rms misfit between the
267 calculated silicon content (from Equation 1) and the fit described by Equation 2 is 2.8 wt% Si,
268 comparable to our estimated (rms) uncertainty on the silicon content calculation. Phase
269 boundaries calculated from Equation 2 are shown in Figure 4, illustrating compatibility with the
270 observed phase boundary crossings in Fe–9Si. The hcp+B2 mixture is stabilized by increasing
271 temperature, increasing silicon content, or decreasing pressure. This equation indicates that near
272 inner core boundary conditions (329 GPa, 6000 K), an Fe–Si alloy containing greater than
273 0.0(21) wt% Si will be stable as a two-phase hcp+B2 mixture. For a temperature of 5500 K, an
274 Fe–Si alloy containing greater than 2.7(19) wt% Si will be an hcp+B2 mixture. The effects of
275 nickel on this phase boundary remain uncertain.

276 Figure 5 illustrates a projection of this result to inner core conditions, for an inner core
277 temperature of 5500 K or 6000 K. At 6000 K, an Fe–Ni–Si alloy containing 6.0(7) wt% Si would
278 match the inner core’s density, based on extrapolating the equation of state of Fischer et al.
279 (2014) and correcting for a Ni/Fe atomic ratio of 0.058 (McDonough 2003), consistent with the
280 findings of Tateno et al. (2015). Figure 5 shows that near modern ICB conditions, the stable
281 structure of an Fe–Si alloy with 6 wt% Si should be an hcp+B2 mixture. This phase boundary
282 shifts to increasing silicon content with decreasing temperature, but an hcp+B2 mixture should
283 be stable for Fe–6Si at 329 GPa for temperatures above ~4900 K.

284 This fit predicts a phase transition in Fe–9Si at 329 GPa and 4350(300) K. This
285 temperature falls intermediate between extrapolations of phase boundaries from Fischer et al.
286 (2013) and earlier studies (Lin et al. 2009; Kuwayama et al. 2009). A recent study (Tateno et al.
287 2015) measured the hcp/hcp+B2 phase boundary in Fe–9Si to over 400 GPa. Their phase
288 boundary implies a transition temperature of ~4600 K at 329 GPa, in agreement with the findings
289 of this study within uncertainty.

290

291

Implications

292 The axial c/a ratio in iron and Fe–Ni–Si alloys is sensitive to volume, temperature, and
293 composition, and it has been parameterized here as a function of these variables based on a meta-
294 analysis of experimental studies spanning a large range of pressures and temperatures. The axial
295 ratio increases with volume, temperature, silicon content, and nickel content. The
296 parameterization of the axial ratio as a function of these variables can be used to calculate the
297 composition of an hcp Fe–Si alloy if its c/a ratio, temperature, and volume (or pressure) are
298 known. Though not a substitute for direct compositional measurements, this method offers a new

299 application of equation of state data, a means to estimate the composition of the high P - T Fe–Si
300 phase in situ, and a mechanism for filling in details of phase diagrams, allowing for more robust
301 extrapolations of phase relations in pressure and temperature.

302 This parameterization allows predictions of the c/a ratio of an Fe–Ni–Si alloy of specified
303 composition at inner core conditions, which are necessary to understand the elastic anisotropy of
304 the hcp alloy (Gannarelli et al. 2005). The experiment-based parameterization presented here can
305 inform future ab initio work relating elastic constants to the c/a ratio, for a better understanding
306 of how seismic anisotropy varies with composition in hcp Fe–Ni–Si alloys.

307 The stability field of an hcp+B2 mixture in Fe–Si alloys at 125 and 145 GPa extends
308 almost to pure iron at high temperatures. This large compositional loop is consistent with silicon
309 being the light element in the Earth's core, based on seismological observations of a large
310 density contrast between the inner and outer core (Dziewonski and Anderson 1981; Kennett et al.
311 1995; Masters and Gubbins 2003). It also implies eutectic melting in the Fe–Si system over a
312 large compositional range.

313 Our calculations of the Fe–Si phase diagram suggest that if silicon is an important part of
314 the core's light element component, then a two-phase hcp+B2 mixture may be stable at inner
315 core conditions. In a two component system, there can only be two stable phases at the ICB
316 (hcp+melt), in which case the hcp structure would be stable in the inner core, but in a ternary or
317 higher order system with additional light element(s) present, hcp and B2 phases could be co-
318 crystallizing in the Earth's inner core along a cotectic. (In this case, the density contrast at the
319 ICB would be attributable mostly to the additional light element(s).) As the inner core grew, it
320 may have crystallized different compositions containing different relative amounts of hcp and B2
321 Fe–Si-rich alloy. The hcp and B2 phases have different anisotropies, so this may lead to

322 variations of anisotropy with depth. The ab initio simulations of Belonoshko et al. (2008)
323 indicate a much stronger anisotropy in bcc Fe than in hcp Fe, though results of other studies
324 (e.g., Tsuchiya and Fujibuchi 2009) are in conflict with this low anisotropy of hcp Fe. Future
325 studies on the anisotropy of bcc-like Fe-alloys at inner core conditions are needed to clarify this
326 issue. Similarly, it is possible that the proposed inner core translation (Alboussi re et al. 2010)
327 could cause hemispherical variations in anisotropy due to variations in phase proportion. In
328 addition to hemispherical and radial variations in phase proportions, the hcp phase will have a
329 different c/a ratio based on its composition and volume, with its anisotropy decreasing as the c/a
330 ratio approaches its ideal value of 1.633. The combination of a two-phase mixture in the inner
331 core and variations in the c/a ratio of hcp phases may help explain the observed seismic
332 anisotropy patterns in Earth's core.

333

334

Acknowledgments

335 We thank Razvan Caracas for useful discussions. We are grateful to the editor for handling this
336 manuscript and to two anonymous reviewers for constructive reviews. This work was supported
337 by a National Science Foundation (NSF) Graduate Research Fellowship, an Illinois Space Grant
338 Consortium Graduate Research Fellowship, an International Centre for Diffraction Data Ludo
339 Frevel Crystallography Scholarship, and an American Association of University Women
340 American Dissertation Fellowship to R.A.F. This work was supported by NSF grant EAR-
341 1427123 to A.J.C.

342

343

References

- 344 Alboussière, T., Deguen, R., and Melzani, M. (2010) Melting-induced stratification above the
345 Earth's inner core due to convective translation. *Nature*, 466, 744–747.
- 346 Allègre, C.J., Poirier, J.-P., Humler, E., and Hofmann, A.W. (1995) The chemical composition of
347 the Earth. *Earth and Planetary Science Letters*, 134, 515–526.
- 348 Anzellini, S., Dewaele, A., Mezouar, M., Loubeyre, P., and Morard, G. (2013) Melting of iron at
349 Earth's inner core boundary based on fast X-ray diffraction. *Science*, 340, 464–466.
- 350 Belonoshko, A.B., Ahuja, R., and Johansson, B. (2003) Stability of the body-centred-cubic phase
351 of iron in the Earth's inner core. *Nature*, 424, 1032–1034.
- 352 Bergman, M.I. (1997) Measurements of electric anisotropy due to solidification texturing and the
353 implications for the Earth's inner core. *Nature*, 389, 60–63.
- 354 Birch, F. (1952) Elasticity and constitution of the Earth's interior. *Journal of Geophysical*
355 *Research*, 57, 227–286.
- 356 Boehler, R., Santamaría-Pérez, D., Errandonea, D., and Mezouar, M. (2008) Melting, density,
357 and anisotropy of iron at core conditions: New X-ray measurements to 150 GPa. *Journal of*
358 *Physics: Conference Series*, 121, 022018.
- 359 Buffett, B.A., and Wenk, H.-R. (2001) Texturing of the Earth's inner core by Maxwell stresses.
360 *Nature*, 413, 60–63.
- 361 Dewaele, A., Loubeyre, P., Occelli, F., Mezouar, M., Dorogokupets, P.I., and Torrent, M. (2006)
362 Quasihydrostatic equation of state of iron above 2 Mbar. *Physical Review Letters*, 97,
363 215504.
- 364 Dorogokupets, P.I., and Oganov, A.R. (2007) Ruby, metals, and MgO as alternative pressure
365 scales: A semiempirical description of shock-wave, ultrasonic, x-ray, and thermochemical
366 data at high temperatures and pressures. *Physical Review B*, 75, 024115.

- 367 Dubrovinsky, L.S., Saxena, S.K., Tutti, F., and Rekhi, S. (2000) In situ X-ray study of thermal
368 expansion and phase transition of iron at multimegabar pressure. *Physical Review Letters*,
369 84, 1720–1723.
- 370 Dziewonski, A.M., and Anderson, D.L. (1981) Preliminary reference Earth model. *Physics of the*
371 *Earth and Planetary Interiors*, 25, 297–356.
- 372 Fischer, R.A., Campbell, A.J., Shofner, G.A., Lord, O.T., Dera, P., and Prakapenka, V.B. (2011)
373 Equation of state and phase diagram of FeO. *Earth and Planetary Science Letters*, 304, 496–
374 502.
- 375 Fischer, R.A., Campbell, A.J., Caracas, R., Reaman, D.M., Dera, P., and Prakapenka, V.B.
376 (2012) Equation of state and phase diagram of Fe–16Si alloy as a candidate component of
377 Earth’s core. *Earth and Planetary Science Letters*, 357–358, 268–276.
- 378 Fischer, R.A., Campbell, A.J., Reaman, D.M., Miller, N.A., Heinz, D.L., Dera, P., and
379 Prakapenka, V.B. (2013) Phase relations in the Fe–FeSi system at high pressures and
380 temperatures. *Earth and Planetary Science Letters*, 373, 54–64.
- 381 Fischer, R.A., Campbell, A.J., Caracas, R., Reaman, D.M., Heinz, D.L., Dera, P., and
382 Prakapenka, V.B. (2014) Equations of state in the Fe–FeSi system at high pressures and
383 temperatures. *Journal of Geophysical Research*, 119, 2810–2827.
- 384 Gannarelli, C.M.S., Alfè, D., and Gillan, M.J. (2005) The axial ratio of hcp iron at the conditions
385 of the Earth’s inner core. *Physics of the Earth and Planetary Interiors*, 152, 67–77.
- 386 Irving, J.C.E., and Deuss, A. (2011a) Stratified anisotropic structure at the top of Earth’s inner
387 core: A normal mode study. *Physics of the Earth and Planetary Interiors*, 186, 59–69.
- 388 Irving, J.C.E., and Deuss, A. (2011b) Hemispherical structure in inner core velocity anisotropy.
389 *Journal of Geophysical Research*, 116, B04307.

- 390 Ishii, M., and Dziewonski, A.M. (2002) The innermost inner core of the earth: Evidence for a
391 change in anisotropic behavior at the radius of about 300 km. Proceedings of the National
392 Academy of Sciences of the United States of America, 99, 14026–14030.
- 393 Ishii, M., and Dziewonski, A.M. (2003) Distinct seismic anisotropy at the centre of the Earth.
394 Physics of the Earth and Planetary Interiors, 140, 203–217.
- 395 Jeanloz, R., and Wenk, H.-R. (1988) Convection and anisotropy of the inner core. Geophysical
396 Research Letters, 15, 72–75.
- 397 Jephcoat, A., and Olson, P. (1987) Is the inner core of the Earth pure iron? Nature, 325, 332–
398 335.
- 399 Jephcoat, A.P., Mao, H.K., and Bell, P.M. (1986) Static compression of iron to 78 GPa with rare
400 gas solids as pressure-transmitting media. Journal of Geophysical Research, 91, 4677–4684.
- 401 Karato, S.-I. (1999) Seismic anisotropy of the Earth's inner core resulting from flow induced by
402 Maxwell stresses. Nature, 402, 871–873.
- 403 Kennett, B.L.N., Engdahl, E.R., and Buland, R. (1995) Constraints on seismic velocities in the
404 Earth from traveltimes. Geophysical Journal International, 122, 108–124.
- 405 Komabayashi, T., Fei, Y., Meng, Y., and Prakapenka, V. (2009) In-situ X-ray diffraction
406 measurements of the γ - ϵ transition boundary of iron in an internally-heated diamond anvil
407 cell. Earth and Planetary Science Letters, 282, 252–257.
- 408 Komabayashi, T., Hirose, K., and Ohishi, Y. (2012) In situ X-ray diffraction measurements of
409 the fcc–hcp phase transition boundary of an Fe–Ni alloy in an internally heated diamond
410 anvil cell. Physics and Chemistry of Minerals, 39, 329–338.

- 411 Kuwayama, Y., Sawai, T., Hirose, K., Sata, N., and Ohishi, Y. (2009) Phase relations of iron–
412 silicon alloys at high pressure and high temperature. *Physics and Chemistry of Minerals*, 36,
413 511–518.
- 414 Lin, J.-F., Heinz, D.L., Campbell, A.J., Devine, J.M., Mao, W.L., and Shen, G. (2002a) Iron–
415 nickel alloy in the Earth’s core. *Geophysical Research Letters*, 29, 1471.
- 416 Lin, J.-F., Heinz, D.L., Campbell, A.J., Devine, J.M., and Shen, G. (2002b) Iron–silicon alloy in
417 Earth’s core? *Science*, 295, 313–315.
- 418 Lin, J.-F., Scott, H.P., Fischer, R.A., Chang, Y.-Y., Kantor, I., and Prakapenka, V.B. (2009)
419 Phase relations of Fe–Si alloy in Earth’s core. *Geophysical Research Letters*, 36, L06306.
- 420 Lythgoe, K.H., Deuss, A., Rudge, J.F., and Neufeld, J.A. (2014) Earth’s inner core: Innermost
421 inner core or hemispherical variations? *Earth and Planetary Science Letters*, 385, 181–189.
- 422 Ma, Y., Somayazulu, M., Shen, G., Mao, H.-k., Shu, J., and Hemley, R.J. (2004) In situ X-ray
423 diffraction studies of iron to Earth-core conditions. *Physics of the Earth and Planetary*
424 *Interiors*, 143–144, 455–467.
- 425 Mao, H.K., Xu, J., and Bell, P.M. (1986) Calibration of the ruby pressure gauge to 800 kbar
426 under quasi-hydrostatic conditions. *Journal of Geophysical Research*, 91, 4673–4676.
- 427 Mao, H.K., Wu, Y., Chen, L.C., and Shu, J.F. (1990) Static compression of iron to 300 GPa and
428 Fe_{0.8}Ni_{0.2} alloy to 260 GPa: Implications for composition of the core. *Journal of Geophysical*
429 *Research*, 95, 21737–21742.
- 430 Masters, G., and Gubbins, D. (2003) On the resolution of density within the Earth. *Physics of the*
431 *Earth and Planetary Interiors*, 140, 159–167.
- 432 McDonough, W.F. (2003) Compositional model for the Earth’s core. In R.W. Carlson, Ed.,
433 *Treatise on Geochemistry*, vol. 2, p. 547–568. Elsevier-Pergamon, Oxford, U.K.

- 434 Modak, P., Verma, A.K., Rao, R.S., Godwal, B.K., Stixrude, L., and Jeanloz, R. (2007) Stability
435 of the hcp phase and temperature variation of the axial ratio of iron near Earth-core
436 conditions. *Journal of Physics: Condensed Matter*, 19, 016208.
- 437 Morelli, A., Dziewonski, A.M., and Woodhouse, J.H. (1986) Anisotropy of the inner core
438 inferred from *PKIKP* travel times. *Geophysical Research Letters*, 13, 1545–1548.
- 439 Ono, S., Kikegawa, T., Hirao, N., and Mibe, K. (2010) High-pressure magnetic transition in hcp-
440 Fe. *American Mineralogist*, 95, 880–883.
- 441 Poupinet, G., Pillet, R., and Souriau, A. (1983) Possible heterogeneity of the Earth's core
442 deduced from *PKIKP* travel times. *Nature*, 305, 204–206.
- 443 Pozzo, M., Davies, C., Gubbins, D., and Alfè, D. (2014) Thermal and electrical conductivity of
444 solid iron and iron–silicon mixtures at Earth's core conditions. *Earth and Planetary Science
445 Letters*, 393, 159–164.
- 446 Reaman, D.M., Daehn, G.S., and Panero, W.R. (2011) Predictive mechanism for anisotropy
447 development in the Earth's inner core. *Earth and Planetary Science Letters*, 312, 437–442.
- 448 Sakai, T., Ohtani, E., Hirao, N., and Ohishi, Y. (2011) Stability field of the hcp-structure for Fe,
449 Fe–Ni, and Fe–Ni–Si alloys up to 3 Mbar. *Geophysical Research Letters*, 38, L09302.
- 450 Sakai, T., Ohtani, E., Kamada, S., Terasaki, H., and Hirao, N. (2012) Compression of
451 $\text{Fe}_{88.1}\text{Ni}_{9.1}\text{Si}_{2.8}$ alloy up to the pressure of Earth's inner core. *Journal of Geophysical Research*,
452 117, B02210.
- 453 Sha, X., and Cohen, R.E. (2006) Thermal effects on lattice strain in ϵ -Fe under pressure. *Physical
454 Review B*, 74, 064103.

- 455 Shahar, A., Ziegler, K., Young, E.D., Ricolleau, A., Schauble, E.A., and Fei, Y. (2009)
456 Experimentally determined Si isotope fractionation between silicate and Fe metal and
457 implications for Earth's core formation. *Earth and Planetary Science Letters*, 288, 228–234.
- 458 Steinle-Neumann, G., Stixrude, L., Cohen, R.E., and Gülseren, O. (2001) Elasticity of iron at the
459 temperature of the Earth's inner core. *Nature*, 413, 57–60.
- 460 Stixrude, L., and Cohen, R.E. (1995) High-pressure elasticity of iron and anisotropy of Earth's
461 inner core. *Science*, 267, 1972–1975.
- 462 Tanaka, S., and Hamaguchi, H. (1997) Degree one heterogeneity and hemispherical variation of
463 anisotropy in the inner core from PKP(BC)–PKP(DF) times. *Journal of Geophysical*
464 *Research*, 102, 2925–2938.
- 465 Tateno, S., Hirose, K., Ohishi, Y., and Tatsumi, Y. (2010) The structure of iron in Earth's inner
466 core. *Science*, 330, 359–361.
- 467 Tateno, S., Hirose, K., Komabayashi, T., Ozawa, H., and Ohishi, Y. (2012) The structure of Fe–
468 Ni alloy in Earth's inner core. *Geophysical Research Letters*, 39, L12305.
- 469 Tateno, S., Kuwayama, Y., Hirose, K., and Ohishi, Y. (2015) The structure of Fe–Si alloy in
470 Earth's inner core. *Earth and Planetary Science Letters*, 418, 11–19.
- 471 Tsuchiya, T., and Fujibuchi, M. (2009) Effects of Si on the elastic property of Fe at Earth's inner
472 core pressures: First principles study. *Physics of the Earth and Planetary Interiors*, 174, 212–
473 219.
- 474 Uchida, T., Wang, Y., Rivers, M.L., and Sutton, S.R. (2001) Stability field and thermal equation
475 of state of ϵ -iron determined by synchrotron X-ray diffraction in a multianvil apparatus.
476 *Journal of Geophysical Research*, 106, 21799–21810.

- 477 Vočadlo, L., Alfè, D., Gillan, M.J., Wood, I.G., Brodholt, J.P., and Price, G.D. (2003) Possible
478 thermal and chemical stabilization of body-centered-cubic iron in the Earth's core. *Nature*,
479 424, 536–539.
- 480 Vočadlo, L., Dobson, D.P., and Wood, I.G. (2009) Ab initio calculations of the elasticity of hcp-
481 Fe as a function of temperature at inner-core pressure. *Earth and Planetary Science Letters*,
482 288, 534–538.
- 483 Wasserman, E., Stixrude, L., and Cohen, R.E. (1996) Thermal properties of iron at high
484 pressures and temperatures. *Physical Review B*, 53, 8296–8309.
- 485 Wenk, H.R., Takeshita, T., Jeanloz, R., and Johnson, G.C. (1988) Development of texture and
486 elastic anisotropy during deformation of hcp metals. *Geophysical Research Letters*, 15, 76–
487 79.
- 488 Yamazaki, D., Ito, E., Yoshino, T., Yoneda, A., Guo, X., Zhang, B., Sun, W., Shimojuku, A.,
489 Tsujino, N., Kunimoto, T., Higo, Y., and Funakoshi, K.-i. (2012) *P-V-T* equation of state for
490 ϵ -iron up to 80 GPa and 1900 K using the Kawai-type high pressure apparatus equipped with
491 sintered diamond anvils. *Geophysical Research Letters*, 39, L20308.
- 492 Yoshida, S., Sumita, I., and Kumazawa, M. (1996) Growth model of the inner core coupled with
493 the outer core dynamics and the resulting elastic anisotropy. *Journal of Geophysical*
494 *Research*, 101, 28085–28103.

495

496

Figure Captions:

- 497 Figure 1: Axial ratio of hcp Fe–Ni–Si alloys as a function of volume and temperature. A: Pure
498 hcp iron. Filled diamonds: Anzellini et al. (2013). Filled squares: Boehler et al. (2008). Filled
499 triangles: Fischer et al. (2011). Filled circles: Yamazaki et al. (2012). Open diamonds: Ono et al.

500 (2010). Open squares: Tateno et al. (2010). Open triangles: Uchida et al. (2001). Open circles:
501 Sakai et al. (2011). × symbols: Dewaele et al. (2006). B: Fe–10Ni alloy. Filled diamonds: Tateno
502 et al. (2012). Filled squares: Lin et al. (2002a). Filled triangles: Komabayashi et al. (2012). Filled
503 circles: Sakai et al. (2011). C: Fe–9Si alloy. Filled diamonds: Fischer et al. (2014). Filled circles:
504 Lin et al. (2002b). Filled triangles: Tateno et al. (2015). All data are color-coded by temperature
505 according to the legend. Curves are calculated from Equation 1, and are shown for the midpoints
506 of the indicated temperature ranges. In part A, they are truncated to not extend outside the
507 stability field of hcp iron (Anzellini et al. 2013; Komabayashi et al. 2009). Error bars are not
508 shown because some studies did not report uncertainties, but they are typically in the range 0.02
509 to 0.3% for the c/a ratio.

510

511 Figure 2: Measured c/a axial ratio of Fe–9Si compared to that of pure iron as a function of
512 temperature. Data on Fe–9Si (grey symbols) are from a heating cycle at ~145 GPa (Fischer et al.
513 2014). Data on pure iron (black symbols) span ~130–155 GPa. Iron data come from a variety of
514 studies (Anzellini et al. 2013; Boehler et al. 2008; Fischer et al. 2011; Tateno et al. 2010), with a
515 single heating cycle shown from each study. Lines are calculated for 145 GPa (based on
516 equations of state of Dewaele et al. (2006) and Fischer et al. (2014)) from Equation 1 (solid line:
517 Fe–9Si; dashed line: pure iron). The trends of the data are parallel, indicating that the c/a ratios
518 of Fe–9Si and pure iron have similar temperature dependences at this pressure.

519

520 Figure 3: Residuals to Equation 1. Symbols are as in Figure 1. A: Pure hcp iron. B: Fe–10Ni
521 alloy. C: Fe–9Si alloy. All data are color-coded by temperature according to the legend.

522

523 Figure 4: Phase boundaries in the Fe–FeSi system calculated using the c/a ratio of intermediate
524 alloys at A: ~125 GPa and B: ~145 GPa. Each data point represents an observation of coexisting
525 hcp and B2 structures in either Fe–9Si (blue diamonds) or Fe–16Si (orange open circles). Data
526 are from Fischer et al. (2012, 2014). The c/a ratio of the hcp phase was used to calculate its
527 composition along the phase boundary using Equation 1. Black crosses indicate upper and lower
528 bounds on the transition for Fe–9Si based on in situ X-ray diffraction measurements (Fischer et
529 al. 2013). Solid black lines are phase boundaries calculated from Equation 2; dashed lines are
530 95% confidence intervals. Error bars in composition are a root mean square misfit.

531

532 Figure 5: Phase diagram of Fe–Si alloys in the inner core, calculated using Equation 2 and shown
533 in pressure-composition space at a fixed temperature of 6000 K (black lines) or 5500 K (grey
534 lines). Solid lines: hcp to hcp+B2 phase boundary. Dashed lines: amount of silicon needed to
535 match the inner core's density at these conditions (Fischer et al. 2014). Yellow bands indicate
536 uncertainties at 6000 K. If silicon is the core's dominant light element, the inner core may be a
537 mixture of hcp and B2 phases.

538

539

540

541

Supplemental Table Captions:

542 Table S1: Compilation of c/a ratios from 15 studies, as a function of temperature, volume, lattice
543 parameter a , and mole fractions of Ni and Si. Uncertainties on the c/a ratio are listed where
544 available.

545

546 Table S2: Variance-covariance matrix describing the fit of c/a as a function of T , V , and
547 composition (Equation 1), with T in Kelvin, V in cm^3/mol , and X_{Si} and X_{Ni} in mole fraction.
548 Diagonal terms describe the variance in each coefficient, while off-diagonal terms describe the
549 covariance between terms. Matrix is symmetric by definition.

550

551 Table S3: Variance-covariance matrix describing the silicon content along the hcp to hcp+B2
552 phase boundary in the Fe–Si system as a function of T and P (Equation 2), with silicon content in
553 weight percent, T in Kelvin, and P in GPa. Diagonal terms describe the variance in each
554 coefficient, while off-diagonal terms describe the covariance between terms. Matrix is symmetric
555 by definition.

556

557

Supplemental Figure Caption:

558 Figure S1: Schematic temperature-composition phase diagrams in the Fe–Si system. A: A wide
559 hcp+B2 two-phase field (red arrow), as shown in this study, allows for a larger compositional
560 contrast (blue arrow) between coexisting solid and melt at inner core boundary pressures. This
561 makes it possible for a Si-rich core to be compatible with seismic observations of a large density
562 contrast between the inner and outer core (e.g., Masters and Gubbins 2003). B: In contrast, a
563 narrow two-phase field would preclude the possibility of a large compositional contrast between
564 coexisting solid and melt in the Fe–Si system, making silicon a less viable candidate for the
565 core's dominant light element.

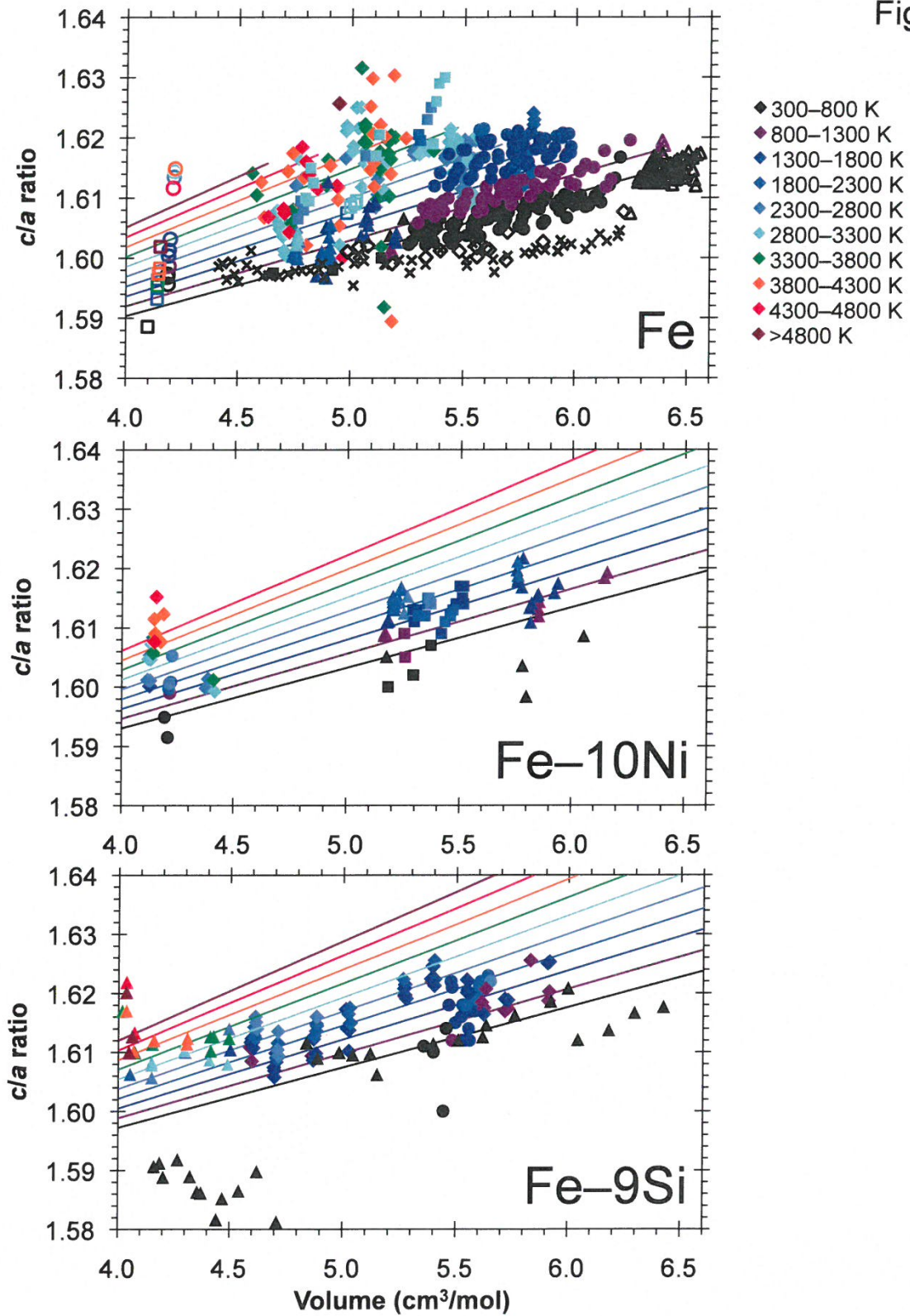
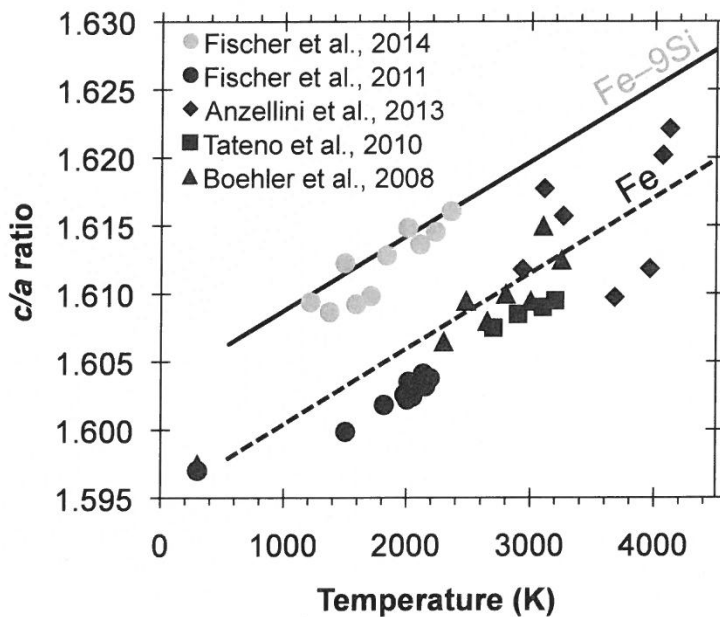


Figure 1
A:

B:

C:

Figure 2



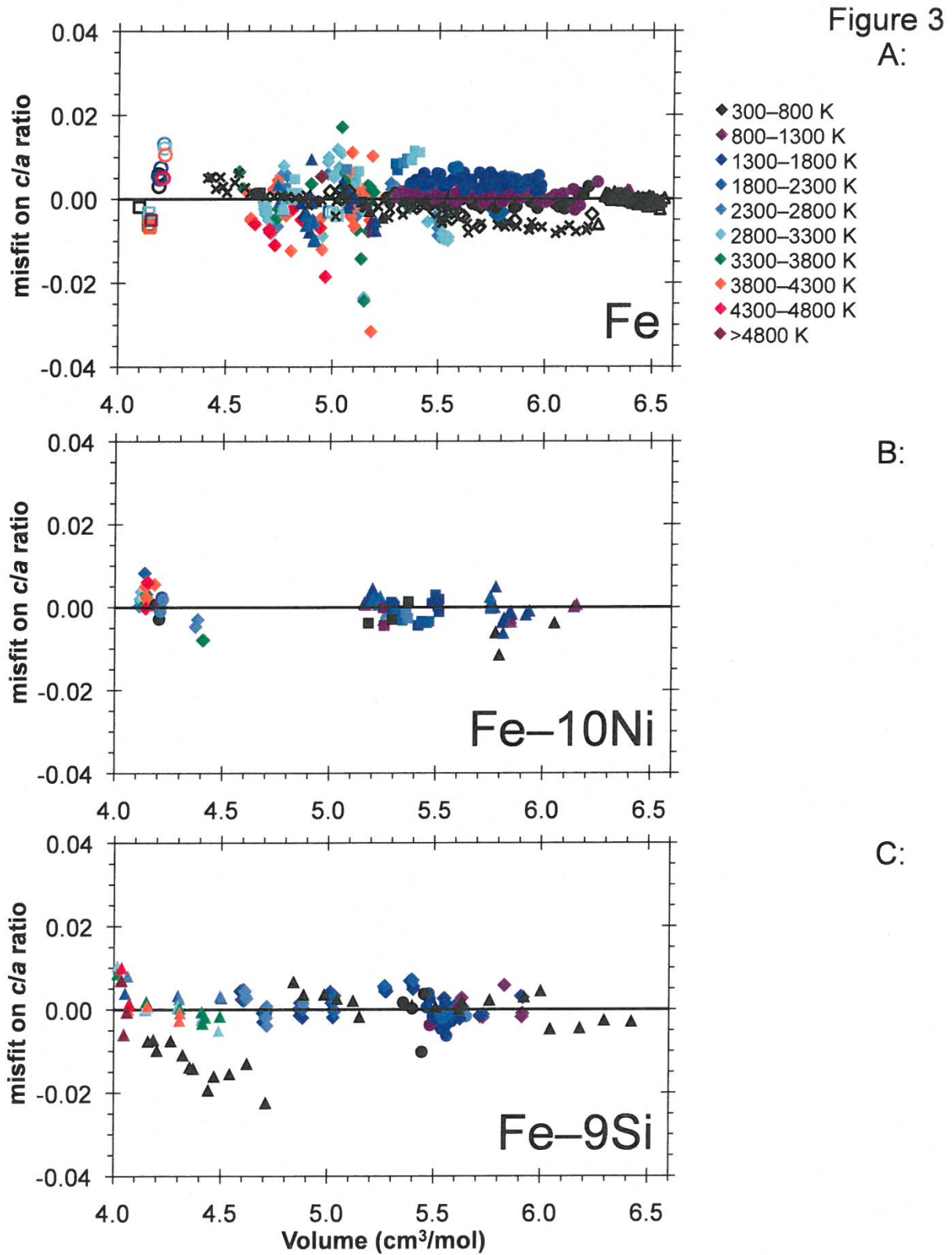


Figure 4

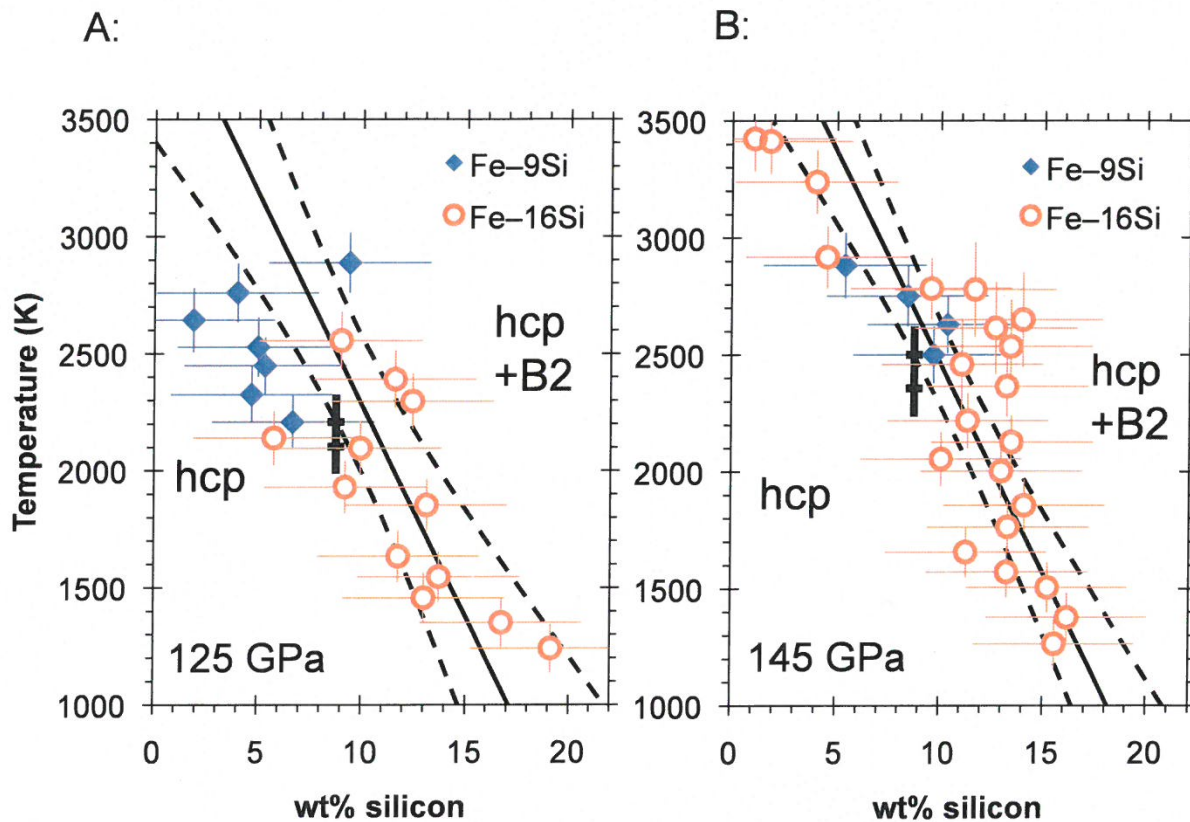


Figure 5

